

Journal of Mechanics of Materials and Structures

**NUMERICAL SIMULATIONS OF MECHANICAL PROPERTIES OF
ALUMINA FOAMS BASED ON COMPUTED TOMOGRAPHY**

Zdzisław Nowak, Marcin Nowak, Ryszard Pęcherski, Marek Potoczek and Romana Śliwa

Volume 12, No. 1

January 2017



NUMERICAL SIMULATIONS OF MECHANICAL PROPERTIES OF ALUMINA FOAMS BASED ON COMPUTED TOMOGRAPHY

ZDZISŁAW NOWAK, MARCIN NOWAK, RYSZARD PECHERSKI,
MAREK POTOCZEK AND ROMANA ŚLIWA

The aim of this paper is to apply the results of microtomography of alumina foam to create a numerical model and perform numerical simulations of compression tests. The geometric characteristics of real foam samples are estimated from tomographic and scanning electron microscopy images. The performance of the reconstructed models is compared to experimental values of elastic moduli. A preliminary analysis of failure strength simulations under compression of alumina foam is also provided.

1. Introduction

Computed tomography is one of several rapidly developing methods of noninvasive testing that plays an important role in medicine and in related diverse engineering applications (e.g., defect detection or the local characterization of a material's microstructure). Starting with an early paper by Bartholomew and Casagrande [1957], which reported the first images characterizing the density of particles in fluidized systems, industrial applications appeared in the 1980s. The development of high speed computers allowed large amounts of data to be processed, which enabled the creation of a new methodology called computed tomography (CT), leading to its widespread use in phase contrast tomography; the reconstruction of the microstructure of diverse cellular materials of polyurethane, metallic and ceramic skeletons, and metal/ceramic composites; and the characterization of void and reinforcement distributions in engineering materials (see [Baruchel et al. 2000] for one of the first comprehensive overviews of the subject). In [Alié et al. 2006], x-ray microtomography measurements coupled with image analysis were applied to study the quality of alumina foams after gel drying and calcinations.

Later, a new methodology was proposed to estimate 3D displacement fields from pairs of images obtained from x-ray computed microtomography. The method was illustrated with an analysis of a compression test on a polypropylene solid foam [Roux et al. 2008]. The presented methodology is also applicable to other kinds of foams (e.g., ceramic foams).

Complex ceramic shapes can be prepared through several methods, such as injection molding, slip casting, or gelcasting combined with a foaming method. If gelcasting techniques were combined with an emulsion template, the fabrication process of highly porous ceramics (60–95%) could be simplified and their strength could be improved. By the gelcasting technique, porous ceramics could satisfy the criteria

Financial support of the Structural Funds in the Operational Program Innovative Economy (IE OP) financed from the European Regional Development Fund Project “Modern material technologies in aerospace industry”, Nr POIG.01.01.02-00-015/08-00 is gratefully acknowledged.

Keywords: Alumina open-cell foam, computed tomography microstructure, Young's modulus, compressive strength of alumina foams.

of homogeneity, reproducibility, reliability, and processability required for complex commercial ceramic foam shapes. The papers by Yang et al. [2011] and Tulliani et al. [2013] review the development and applications of the gelcasting technique.

In [Nowak et al. 2013; 2015] and [Fey et al. 2015], the application of CT is used for the analysis of microstructural morphology and the mechanical and thermal characterization of alumina gelcast foams manufactured with the use of environmentally friendly gelling agents. In the literature, there is little data of the elastic properties of such kinds of foams. Therefore, the aim of this paper is to present a numerical model of an open-cell foam with different porosities and discuss the estimation methodology of Young's moduli. The applied CT approach based on finite element analysis is hard and time consuming; therefore, the work on an optimized generation of the calculation model is essential.

The structure of cellular alumina can be characterized by its cell topology (open), morphology (i.e., cell size and cell spherical shape), and relative density (i.e., volume of the solid cell wall material divided by the volume of the cellular material). The open-cell foam is a structure where the pores form interconnected networks [Potoczek 2008].

It should be noticed that cellular ceramic materials are characterized by a low density combined with outstanding mechanical, thermal and acoustic properties [Gibson and Ashby 1999]. As a consequence of their interesting properties, open-cell foams can be used in lightweight constructions, combining energy absorption, structural damping, sound absorption and heat insulation. In the literature, the models of cellular materials are based on simplified skeleton geometries, notably the Gibson and Ashby cubic cell [Gibson and Ashby 1999]. The simplification of the real cellular material structure enables an analytical approach, reducing the requirements on computer hardware, (e.g., [Michalska and Pęcherski 2003], where further references can be found). However, the last few years have opened new research possibilities, such as numerical analysis based on microcomputed tomography images applied to the mechanical investigation of cellular materials.

The numerical parameters which are needed to build the unit cell model are based on the data obtained from microtomography images of real foam. Using the procedures described in [Nowak et al. 2013], the analysis of the microtomography images shows that the alumina foams are composed of approximately spherical cells interconnected by circular windows [Potoczek 2008].

In this paper, a novel methodology is proposed to establish the cell and windows distribution from 2D microcomputed tomography (μ CT) scanning images of real alumina foam and how to reconstruct the virtual model of foam geometry. Then the two-step mesh method is employed to discretize the geometrical model by selecting an appropriate node, and finally the FEM of alumina foam is established directly. This approach is used to calculate the compression performance of alumina foam with porosity 74%, 86% and 90%. The calculation of alumina foam can reflect the mechanical behavior in the compression process of open-cell foams.

Elastic properties are predicted and compared with experimental data. The skeleton material of the alumina foam is assumed to be isotropic and linearly elastic. In numerical simulations of the compression test on alumina foam, the bottom surface of the sample is fully constrained and the top surface of the sample is moved parallel to the z-axis. The Young's modulus is estimated by numerically simulating uniaxial compression of the alumina foam for different values of porosity. A comparison of experimental data [Potoczek 2008] with numerical and analytical predictions [Gibson and Ashby 1999] of Young's modulus for Al_2O_3 ceramic foams of different porosity is presented.

2. Analysis of foam structure using microtomography

A picture of foam, which was produced by gelcasting combined with a foaming method [Potoczek 2008; Ortega et al. 2006] with 86% porosity is presented in Figure 1. The morphology of alumina foams manufactured by gelcasting is composed of approximately spherical cells interconnected with windows.

The microstructure studies of alumina foam with a porosity of 86% are carried out using the computed x-ray microtomograph SkyScan 1174. In order to obtain images with an optimal ratio of resolution to the dimensions of the foam sample, the pixel size is assumed to be equal to $8.08 \mu\text{m}$. As a result, the series of cross-section images of the foam structure (approximately 1100) with dimensions 1536×1164 pixels were obtained (see Figure 2). The size of the pixel is also compared to the smallest thickness of cell wall. In the alumina foam with a porosity of 86%, this thickness is about $30 \mu\text{m}$, which in terms of pixels gives the value of 4 px. This assumption gives the detailed structure of the foam without neglecting its relevant characteristics.

2A. Computation of porosity. In the first step, all of the cross-section images of the foam are converted to grayscale images where 0 represents the black color, while the value of 255 defines the white color. Next, the threshold value of phase separation (equal to 75) is determined and applied to the series of images. Each pixel with a value less than 75 was included in the pores of the foam (black), while pixels with a value greater than or equal to 75 was included in the skeleton of the foam (white), see Figure 3).

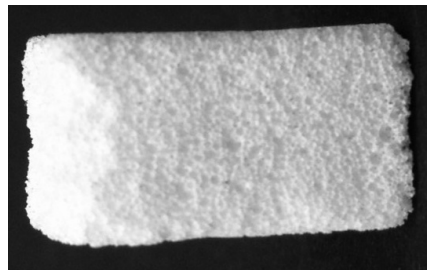


Figure 1. An example of real alumina 86% porosity foam produced by gelcasting.



Figure 2. Images of cross-sections of the alumina foam with porosity of 86% obtained using computer microtomography: cross-section of the foam at the level $\frac{1}{4}$ of its height (left), cross-section of the foam at the level $\frac{1}{2}$ of its height (right) [Nowak 2014].

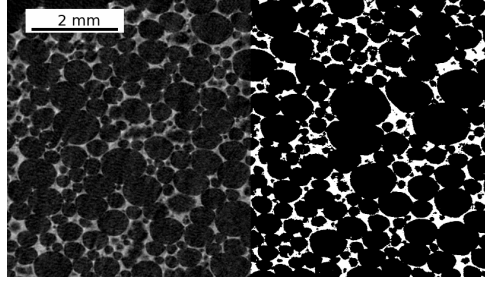


Figure 3. Image of cross-section of alumina foam with porosity of 86% after process of separation of two phases: white color — foam skeleton, black color — foam pores.

The threshold of phase separation is determined by comparing the calculated porosity of the foam sample according to (2-1) to the value measured experimentally. If those two porosities are equal, the value of threshold was chosen correctly.

Equation (2-1) gives the porosity of a cuboid shape sample constructed of cross-sections images and takes the form

$$\phi = \frac{\sum_{k=1}^N \sum_{i=a_1}^{a_2} \sum_{j=b_1}^{b_2} \text{pix}(k, i, j)}{\sum_{k=1}^N \sum_{i=a_1}^{a_2} \sum_{j=b_1}^{b_2}}, \quad (2-1)$$

where N is equal to the number of analyzed images, i and j are the coordinates of the center of pixel, and (a_1, a_2) and (b_1, b_2) are the minimum and maximum coordinates of pixel in horizontal and vertical direction, respectively. The function $\text{pix}(k, i, j)$ is expressed by the formula

$$\text{pix}(k, i, j) = \begin{cases} 1 & \text{if } \text{pix}(k, i, j) < 75, \\ 0 & \text{if } \text{pix}(k, i, j) \geq 75. \end{cases} \quad (2-2)$$

The presented formula of porosity (2-1) depends on the given values of the parameters a_1 , a_2 , b_1 , and b_2 , which determine the minimum and maximum coordinates of the pixels and the number of analyzed images N . In other words, the porosity depends on the calculated volume of the sample. When the volume is larger, the calculated porosity is closer to the value obtained experimentally (Figure 4). For values of $a > 2.0$ mm, where a represents the dimension of the side of the cube, it can be concluded that the effect of the volume change is negligible. Thus, the minimum size of representative volume element (RVE) for foam with a porosity of 86% should be greater than or equal to 2.0 mm.

2B. Computation of cell and window radii. The radii of the cells and windows in the analyzed foam based on cross-section images were obtained with a detection algorithm [Atherton and Kerbyson 1999], available in the MATLAB image processing toolbox. The results of the performed calculations using the program MATLAB are depicted in Figure 5.

We also developed our own procedure for detecting the distribution of the radii of cells. Calculations were carried out in two steps. The first step involves the detection of circular areas with a maximum radius equal to 40 pixels. The second step involves the remaining size of cells. Detection of cells using our procedure is shown in Figure 6. Calculations were made using the open source library PIL (Python Imaging Library) for the Python programming language.

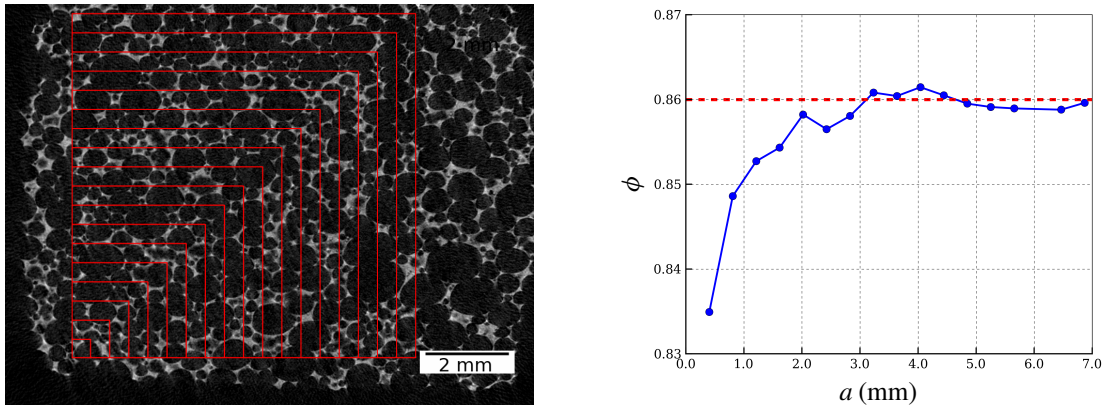


Figure 4. The edges of the square areas for computation of porosities (left). Effect of the size of a cubic volume with side a on the calculated porosities in case of sample with average porosity 86% (right).

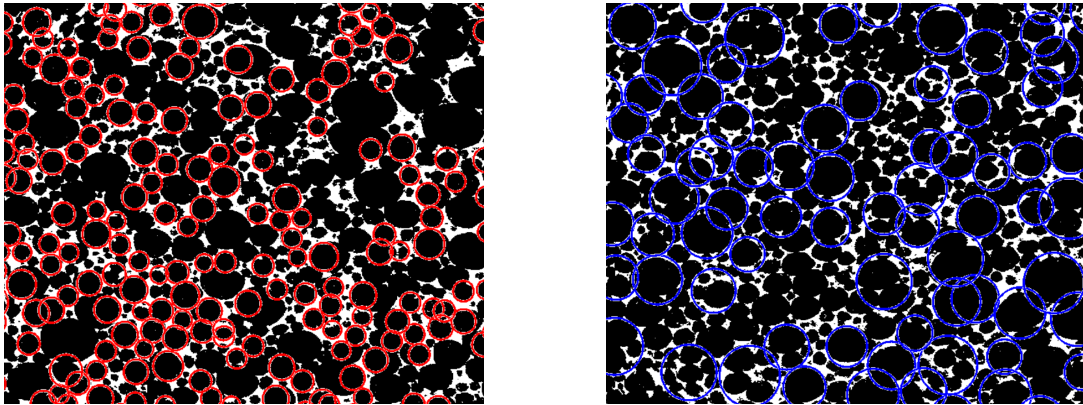


Figure 5. Detection of cells in a foam sample for a flat picture μ CT with the use of MATLAB for radii smaller than 40 px (left) and greater than 40 px (right).

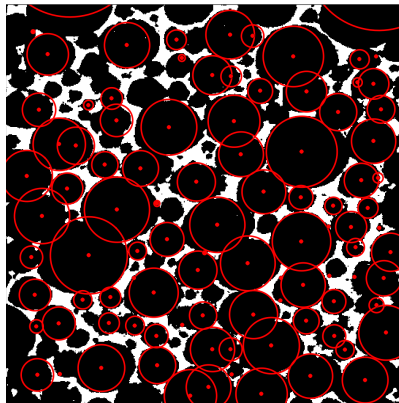


Figure 6. Detection of cells in a foam sample for a picture μ CT using the developed algorithm.



Figure 7. Two situations of two circles: (left) disjoint circles and (right) circles intersecting at two points.

The computed edges of the cells give a set of overlapping circles, for which two situations can be distinguished (Figure 7). The circles may be separate or intersect at two points. The size of the overlap for the two circles describes the parameter k .

By knowing the coordinates of the center of each circle and its radius, the radius of the window r_w can be described using the formula

$$r_w = \frac{\sqrt{2k(-\frac{1}{2}k + r_c^a)(-\frac{1}{2}k + r_c^b)(-k + r_c^a + r_c^b)}}{-k + r_c^a + r_c^b}, \quad (2-3)$$

where r_c^a and r_c^b are the radii of circles.

When the circles intersect, the parameter k determines the size of the overlap. For neighboring circles that do not intersect, the parameter k determines the thickness of the cell wall. The parameter k is given by

$$k = r_c^a + r_c^b - \sqrt{(x_b - x_a)^2 + (y_b - y_a)^2}, \quad (2-4)$$

where (x_a, y_a) and (x_b, y_b) are the coordinates of the center of circles.

As a result, the distribution of the cell radius, window radius and the wall thickness were obtained (Figure 8).

A similar study was conducted for foam having a porosity of 74% and 90%. For the obtained distribution of the cell radius and window radius, the probability density functions were proposed. Due to the lack of symmetry in the presented results (Figure 8), the log normal distribution function is assumed. The log normal distribution is a continuous distribution in which the logarithm of a variable has a normal distribution. Thus, its probability density function, f , can be written as

$$f(x) = \frac{1}{x\sigma_{\log}\sqrt{2\pi}} \exp\left[-\frac{(\ln(x) - \mu_{\log})^2}{2\sigma_{\log}^2}\right]. \quad (2-5)$$

The parameters for this distribution (σ_{\log} and μ_{\log}) are determined by least squares method. Figure 9 shows the density of the probability distribution for the cell radius, r_c , and the window radius, r_w . When the porosity of the foam increases the mean value of the cell, the windows radius of the foam also increases.

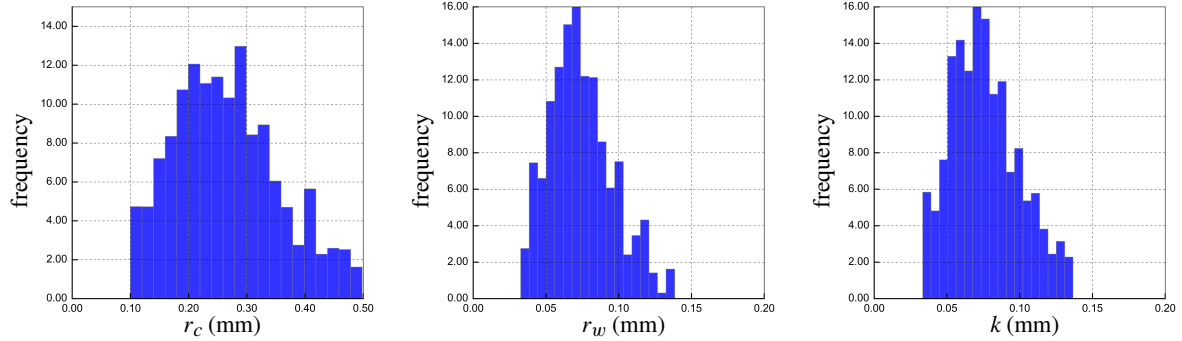


Figure 8. The frequency distribution for the foam sample with 86% porosity as a function of cells radius (left), window radius (center), and wall thickness (right).

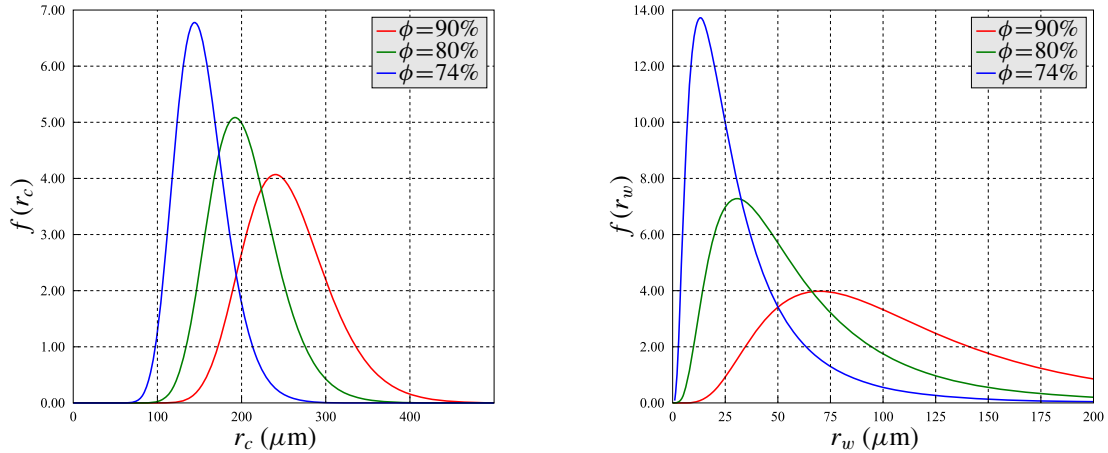


Figure 9. The density of the log-normal probability function for the radius of the cells of the foam (left) and the radius of the windows of the foam (right). Distribution parameters were determined using the least squares method.

porosity (%)	$\mu_{\log} (\mu\text{m})$	$\sigma_{\log} (\mu\text{m})$
90	256	80
80	190	33
74	78	32

Table 1. The summary of results for the mean (μ_{\log}) and standard deviation (σ_{\log}) parameters of the log-normal density function as a function of foam porosity.

A detailed list of the computed parameters for the density of the log-normal probability function is shown in Table 1.

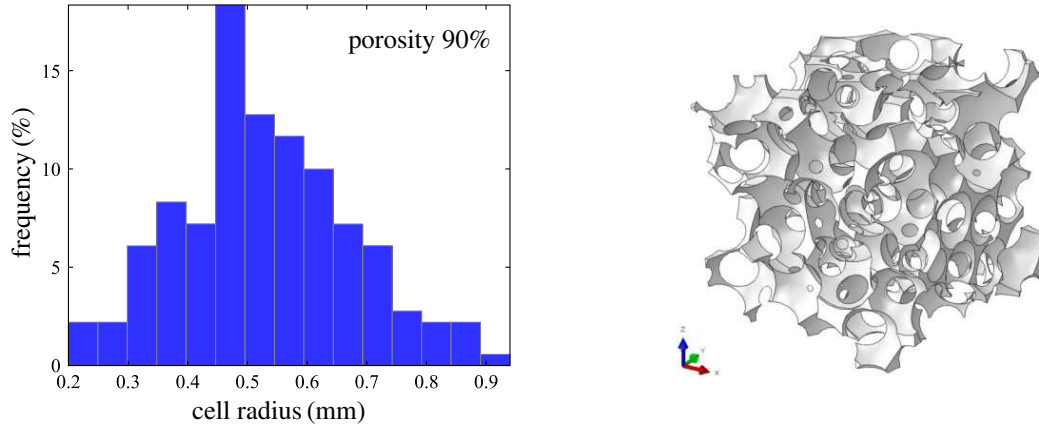


Figure 10. Generated foam structure with 90% porosity: histogram of cell size distribution (left); general view of the foam structure (right).

3. Numerical model of the geometry of open-cell foam with random cell structure

The structure of real foam is very complex, as shown in the 3D picture of alumina foam with 86% porosity obtained by the gelcasting method (Figure 1). The structure of the foam needs to be simplified. This is done by using a model with a random microstructure, which approximates the distribution and shape of the pores in real foam.

The process is based on impacted bubble simulations of random cells, which generates a foam skeleton that is representative of actual foam microstructures. The geometry of ceramic foams can be generated in three steps:

- (1) Diameters of spherical bubbles and windows are estimated from microtomography, see Section 2B.
- (2) Coordinates for the centers of the spherical bubbles are produced by Python scripts [Nowak 2014].
- (3) The intersecting bubbles are subtracted from the bulk volume of any shape.

The initial data for generating the numerical model for the distribution (2-5), the assumed maximal and minimal values of cell diameter (r_{\min} and r_{\max}) for foams of porosity 74%, 86% and 90%, and the assumed number of bubbles are presented in the paper [Nowak et al. 2013]. The particular generated foam structure is illustrated in Figure 10.

4. Finite element modeling

Simulating a compression test by means of a finite element modeling of the random alumina foam microstructure allows us to obtain valuable information about the kinematic state of its structure at some of the test stages. The challenge is then to mesh a representative foam volume to obtain a optimal number of degrees of freedom.

4A. Finite elements mesh generation. The volumetric meshing techniques based on tomographic images uses the natural discretization of the image by voxels. In this case, each voxel lying in the solid region would correspond to an 8-node cubic element. This technique, known as the voxel-element technique, can be easily implemented and does not require any additional expense for mesh generation.

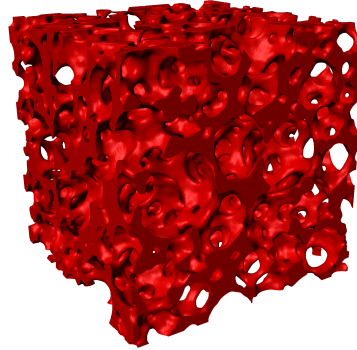


Figure 11. An example of rendered alumina 86% porosity foam.

finite element mesh	(a)	(b)	(c)	(d)
average element size	$\frac{1}{5}r_c$	$\frac{1}{10}r_c$	$\frac{1}{20}r_c$	$\frac{1}{40}r_c$
number of elements	24446	101857	203678	326599
number of degrees of freedom	53404	192294	363157	562621

Table 2. The parameters of four generated finite element mesh networks and the numbers of elements and variables in the alumina 90% porosity foam.

But using this method with a large volume would generate a mesh with millions of nodes, beyond the maximum required for convergence purposes. In another approach, an intermediate step is necessary before meshing the solid volume. In this work, the creation of surface models from the tomographic data is carried out automatically with the help of the advancing front method provided by the ScanIP software [ScanIP 2014], see Figure 11. The element type is C3D10 from the ABAQUS commercial code [ABAQUS 2013]. It is a 10-node tetrahedron with quadratic interpolation. Such second-order elements provide higher accuracy than first-order elements for problems that involve complex stress fields. They capture stress concentrations more effectively and are very effective in bending-dominated problems. The dependence of the number of elements and the number of degrees of freedom on the average size of tetrahedron elements in the case of alumina foam with 90% porosity is presented in Table 2.

Finally, the node coordinates information and element information are written into the INP file, and imported into the ABAQUS to calculate the result. The example of meshed alumina 90% porosity foam used in simulations is shown in Figure 12.

4B. Boundary conditions. The displacement boundary conditions are assumed. In a real uniaxial compression test, the bottom sample surface remains fixed and the top one is moved parallel to the z-axis while the lateral surfaces are free of constraint.

4C. Bulk material properties. It is assumed that the bulk material of alumina foam exhibits an elastic behavior. The model describing the behavior of the considered alumina foam is defined in the elastic range by Hooke's law. Two parameters are needed to calibrate this law: Young's modulus and Poisson's

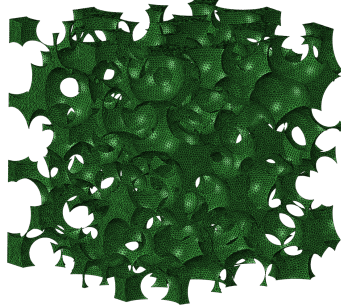


Figure 12. An example of meshed alumina 90% porosity foam used in simulations.

ratio. The following material data for Al_2O_3 have been retained: a Young's modulus $E_0 = 370$ GPa and a Poisson's ratio $\nu = 0.22$.

5. Size of the elementary representative volume

The elementary volume must be large enough to be representative of the overall behavior of the foam. In practice, the elementary volume size is limited, first by the tomography resolution and second by the hardware memory available to generate the mesh and to compute the model. To study the effect of the size of the elementary volume, we extracted regions with different sizes and meshed them with the same mesh density. Different cubic subvolumes with side lengths from 0.1 to 3.0 mm with step size of 0.05 mm were selected. All these volumes are meshed with a mean element volume $V_{el} = 0.08$ mm³ for the model with an average porosity of 90%.

Each marked point on the obtained curves corresponds to one numerical simulation of the uniaxial compression test. This leads to 150 independent numerical simulations (30 simulations per one sample). To manage this task, a special Python script for ABAQUS/CAE was developed. In the repetitive loop, the following steps are taken:

- (a) The geometry based on tomographic images of a given size (from 0.6 mm to 2.5 mm) is created using ScanIP [2014].
- (b) The finite element model is created using ABAQUS/CAE.
- (c) The numerical simulation is performed using ABAQUS/Standard.

Completion of all numerical simulations took about two weeks. The reason for this is the nonlinearly increasing number of elements needed to discretize given sample during the repetitive loop. For example, with an Intel workstation 8x CPU, 2.66 MHz with 12Gb RAM, the numerical simulation of the 0.6 mm size sample took a few seconds and for the 2.5 mm size sample took a few hours.

The calculated Young's modulus normalized by the matrix Young's modulus (E/E_0 , where E_0 is for alumina matrix) and the porosity of the different models are presented in Figure 13. The calculated normalized Young's modulus E/E_0 varies between 0.003–0.019. The sample standard deviation of the calculated normalized Young's modulus is bounded within the limits of 0.003 and 0.014, see Figure 14 (left). On the other hand, the sample standard deviation of the calculated porosity varies from

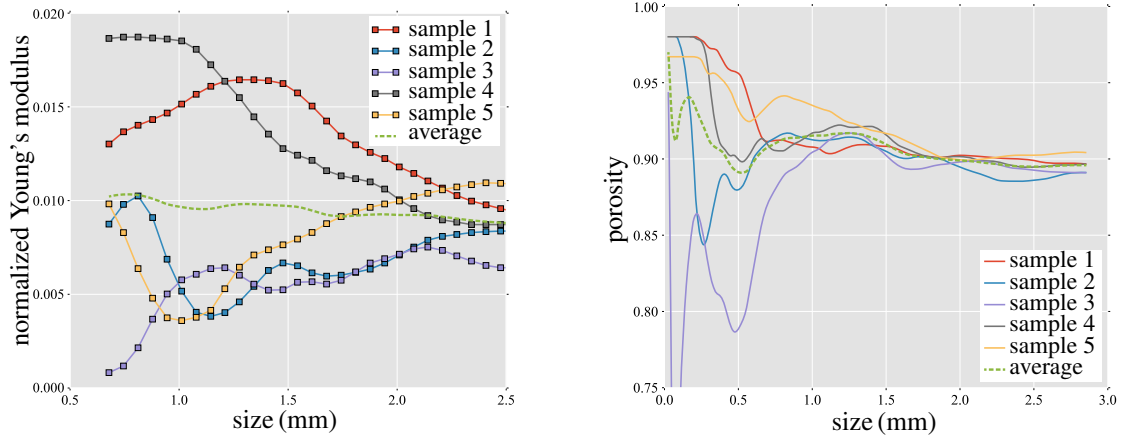


Figure 13. The calculated normalized Young's modulus and the porosity of the samples with average porosity 90% as a function of sample size: normalized Young's modulus (left) and porosity (right).

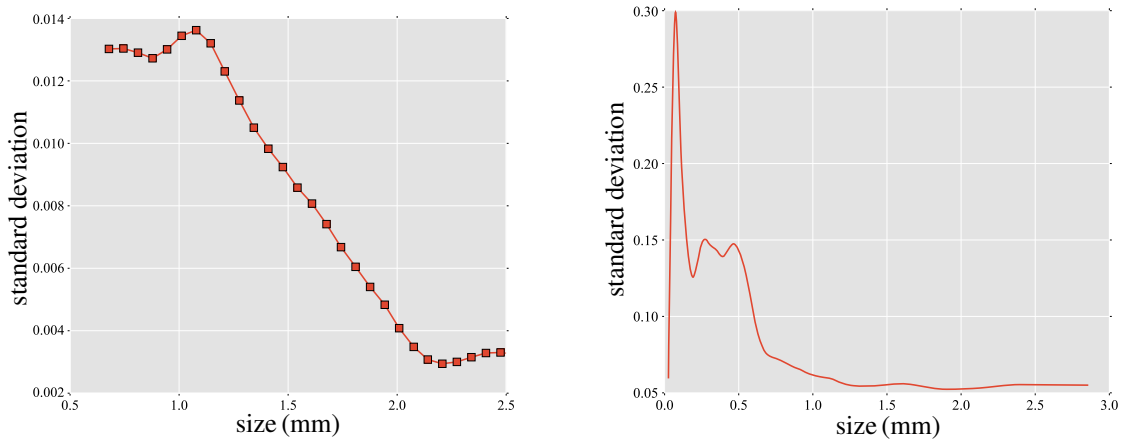


Figure 14. The sample standard deviation of the calculated normalized Young's modulus presented in Figure 13 (left) and of the porosity presented in Figure 13 (right) as a function of the sample size.

0.05 to 0.30, see Figure 14 (right). However, the model with a sample size less than 2.0 mm is several times faster than the FE computation and at least four times faster for the model creation. So, the sample with the size 2.0 mm seems to be a good trade-off between the representativity of the model and the macroscopic accuracy.

6. Summary and conclusions

The modeling methodology of the mechanical behavior of cellular materials was proposed and validated. The actual microstructure of ceramic foam was obtained by processing microtomographic data. The alumina skeleton of the foam was meshed with tetrahedral finite elements. Using the elastic constitutive

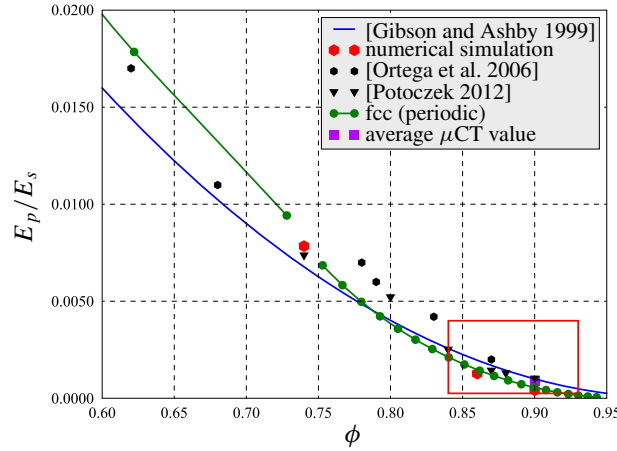


Figure 15. The comparison of numerically predicted normalized Young’s modulus for the random model, the periodic model, and the analytical results of [Gibson and Ashby 1999] as a function of porosity with the experimental data from [Potoczek 2012; Ortega et al. 2006] and the numerical prediction of the μ CT result presented as a slightly oscillating average-value line varying in sample size in Figure 13 (left).

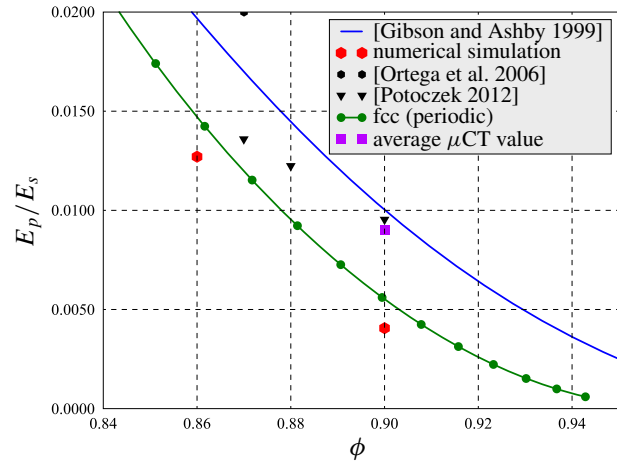


Figure 16. The magnified section of Figure 15.

equations of the bulk material, the uniaxial compression test was simulated. The ABAQUS FEM program [ABAQUS 2013] was used to numerically predict the response of alumina foam under compression. The macroscopic response and the local deformation mechanisms were correctly captured.

A comparison of the normalized Young’s modulus and the numerical predictions for the random model with the experimental data for alumina foams obtained by gelcasting [Potoczek 2012; Ortega et al. 2006] is presented in Figure 15. A comparison with the results of the numerical simulation for the periodic structure of fcc type [Nowak 2014] is also displayed.

In Figure 16, the magnified section of Figure 15 containing the results of the numerical simulations for a periodic structure of the skeleton, the random structure of the skeleton, and for the average μ CT

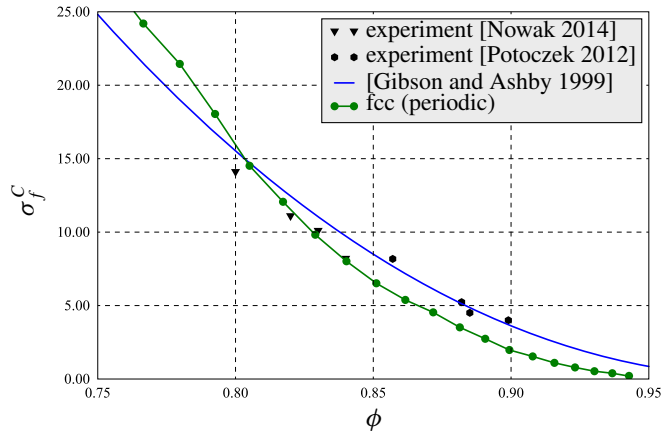


Figure 17. The comparison of numerically predicted failure strength for the periodic fcc model as a function of porosity with the experimental data from [Potoczek 2012; Nowak 2014] and the analytical results of [Gibson and Ashby 1999].

value versus the experimental data is shown. It is visible that the discrepancy between all displayed data is very large, what seems to be typical for low density ceramic foams. At the same time, it can be also observed that the difference between the predicted values of the relative Young's modulus for the periodic and random structure of the skeleton is not significant, e.g., for the porosity $\phi = 0.90$ it is equal to 27%. This observation leads to the hypothesis that the numerical simulation of the deformation process under compression until failure performed for the periodic structure of fcc type, see Figure 17, can provide an estimation of the failure strength σ_f^C for real alumina foams considered in the paper. The advantage of such an approach lies in its low computational cost. The numerical simulations of the failure processes in alumina foam with random structure, which are much more time consuming, are under development.

The present approach can be very useful for designing cellular materials. Indeed, it enables the prediction of the elastic properties of the ceramic foam with feasible microstructures in order to obtain expected mechanical properties.

The novelty of the present paper is the application of the interconnected cell random model of the open-cell foam in simulations of elastic behavior at the microlevel. Using this model, it is possible to estimate the stress and strain fields in the ceramic phase. It is also possible to estimate the macroscopic properties of the foam as functions of the porosity.

The presented numerical approach in the modeling of open-cell foams has some limitations, which should be discussed. The influence of the mesh quality is not mentioned. It is clear that the accuracy of the finite element calculation depends on the quality of tetrahedral elements. Degenerated tetrahedrons with small volumes may lead to large local errors. For a complex foam structures, degenerated elements can not always be avoided. To eliminate them completely, each degenerated element has to be treated separately, which is a cumbersome operation.

In conclusion:

- The numerical model of real Al_2O_3 foam predicting the dependency of Young's modulus while varying porosity within the range from 60% to 95% is discussed and the comparison with experimental data is shown in Figure 15.

- The study of different unit cell sizes, Figure 13, shows that the random representative unit cell reflects the behavior of real Al_2O_3 foams produced by the gelcasting method in a satisfactory way.
- The results of the analysis of failure strength for the periodic skeleton structure of fcc type as a function of porosity are discussed, Figure 17.
- The new results obtained in the paper make a foundation for the development of an energy-based limit criterion of ceramic foams with the application of peridynamic states approach, proposed by Silling [2000] and, as a matter of fact, indicated much earlier by Gabrio Piola [dell’Isola et al. 2015]. The important role the criterion plays can be seen in the formula for critical energy density [Foster et al. 2011]:

$$\omega_c = \frac{4G}{\pi \delta^4}, \quad (6-1)$$

where G denotes energy release rate and δ is a material parameter corresponding to the size of a horizon in peridynamic simulations. The analysis of foam microstructures presented in the paper appears to be useful in estimating the parameter δ .

References

- [ABAQUS 2013] “ABAQUS/Standard user’s manual”, Dassault Systemes, Providence, RI, 2013. Version 6.13.
- [Alié et al. 2006] C. Alié, F. Ferauche, A. Léonard, S. Lambert, N. Tcherkassova, B. Heinrichs, M. Crine, P. Marchot, E. Loukine, and J. Pirard, “Pd-Ag/SiO₂ xerogel catalyst forming by impregnation on alumina foams”, *Chem. Eng. J.* **117**:1 (2006), 13–22.
- [Atherton and Kerbyson 1999] T. J. Atherton and D. J. Kerbyson, “Size invariant circle detection”, *Image Vision Comput.* **17**:11 (1999), 795–803.
- [Bartholomew and Casagrande 1957] R. N. Bartholomew and R. M. Casagrande, “Measuring solids concentration in fluidized systems by gamma-ray absorption”, *Ind. Eng. Chem.* **49**:3 (1957), 428–431.
- [Baruchel et al. 2000] J. Baruchel, J.-Y. Buffiere, E. Maire, P. Merle, and G. Peix, *X-ray tomography in material sciences*, Hermes Science, Paris, 2000.
- [dell’Isola et al. 2015] F. dell’Isola, U. Andreaus, and L. Placidi, “At the origins and in the vanguard of peridynamics, non-local and higher-gradient continuum mechanics: an underestimated and still topical contribution of Gabrio Piola”, *Math. Mech. Solids* **20**:8 (2015), 887–928.
- [Fey et al. 2015] T. Fey, B. Zierath, P. Greil, and M. Potoczek, “Microstructural, mechanical and thermal characterization of alumina gel-cast foams manufactured with the use of agarose as gelling agent”, *J. Porous Mater.* **22**:5 (2015), 1305–1312.
- [Foster et al. 2011] J. T. Foster, S. A. Silling, and W. Chen, “An energy based failure criterion for use with peridynamic states”, *Int. J. Multiscale Comput. Eng.* **9**:6 (2011), 675–688.
- [Gibson and Ashby 1999] L. J. Gibson and M. F. Ashby, *Cellular solids, structure and properties*, 2nd ed., Cambridge University Press, 1999.
- [Michalska and Pęcherski 2003] J. M. Michalska and R. B. Pęcherski, “Macroscopic properties of open-cell foams based on micromechanical modelling”, *Technische Mechanik* **23**:24 (2003), 234–244.
- [Nowak 2014] M. Nowak, *Analiza deformacji i zniszczenia struktur komórkowych w zastosowaniu do symulacji procesu infiltracji pianki korundowej ciekłym metalem*, Ph.D. thesis, 2014, available at http://www.ippt.pan.pl/_download/doktoraty/2014nowak_m_doktorat.pdf.
- [Nowak et al. 2013] M. Nowak, Z. Nowak, R. B. Pęcherski, M. Potoczek, and R. Śliwa, “On the reconstruction method of ceramic foam structures and the methodology of Young modulus determination”, *Arch. Metall. Mater.* **58** (2013), 1219–1222.
- [Nowak et al. 2015] Z. Nowak, M. Nowak, R. B. Pęcherski, M. Potoczek, and R. E. Śliwa, “Mechanical properties of the ceramic open-cell foams of variable cell sizes”, *Arch. Metall. Mater.* **60**:3 (2015), 1957–1963.

- [Ortega et al. 2006] F. S. Ortega, J. A. Rodrigues, and V. C. Pandolfelli, “Elastic modulus of gelcast cellular ceramics at high temperatures”, *Am. Ceram. Soc. Bull.* (2006), 9101–9106.
- [Potoczek 2008] M. Potoczek, “Gelcasting of alumina foams using agarose solutions”, *Ceram. Int.* **34**:3 (2008), 661–667.
- [Potoczek 2012] M. Potoczek, “Kształtowanie mikrostruktury piankowych materiałów korundowych”, Rzeszów University of Technology, Rzeszów, Poland, 2012.
- [Roux et al. 2008] S. Roux, F. Hild, P. Viot, and D. Bernard, “Three-dimensional image correlation from X-ray computed tomography of solid foam”, *Compos. A* **39**:8 (2008), 1253–1265.
- [ScanIP 2014] “ScanIP”, 2014, available at www.simpleware.com/software/scanip. Version 7.0.
- [Silling 2000] S. A. Silling, “Reformulation of elasticity theory for discontinuities and long-range forces”, *J. Mech. Phys. Solids* **48**:1 (2000), 175–209.
- [Tulliani et al. 2013] J.-M. Tulliani, M. Lombardi, P. Palmero, M. Fornabaio, and L. J. Gibson, “Development and mechanical characterization of novel ceramic foams fabricated by gel-casting”, *J. Eur. Ceram. Soc.* **33**:9 (2013), 1567–1576.
- [Yang et al. 2011] J. Yang, J. Yu, and Y. Huang, “Recent developments in gelcasting of ceramics”, *J. Eur. Ceram. Soc.* **31**:14 (2011), 2569–2591.

Received 29 Feb 2016. Revised 4 Aug 2016. Accepted 4 Nov 2016.

ZDZISŁAW NOWAK: znowak@ippt.pan.pl

Institute of Fundamental Technological Research, Polish Academy of Sciences, Pawińskiego 5B, 02-106 Warsaw, Poland

MARCIN NOWAK: nowakm@ippt.pan.pl

Institute of Fundamental Technological Research, Polish Academy of Sciences, Pawińskiego 5B, 02-106 Warsaw, Poland

RYSZARD PECHERSKI: rpecher@ippt.pan.pl

Institute of Fundamental Technological Research, Polish Academy of Sciences, Pawińskiego 5B, 02-106 Warsaw, Poland

MAREK POTOCZEK: potoczek@prz.edu.pl

Faculty of Chemistry, Rzeszów University of Technology, 35-959 Rzeszów, Poland

ROMANA ŚLIWA: rsliwa@prz.edu.pl

Faculty of Mechanical Engineering and Aeronautics, Rzeszów University of Technology, 35-959 Rzeszów, Poland

JOURNAL OF MECHANICS OF MATERIALS AND STRUCTURES

msp.org/jomms

Founded by Charles R. Steele and Marie-Louise Steele

EDITORIAL BOARD

ADAIR R. AGUIAR	University of São Paulo at São Carlos, Brazil
KATIA BERTOLDI	Harvard University, USA
DAVIDE BIGONI	University of Trento, Italy
YIBIN FU	Keele University, UK
IWONA JASIUK	University of Illinois at Urbana-Champaign, USA
C. W. LIM	City University of Hong Kong
THOMAS J. PENCE	Michigan State University, USA
GIANNI ROYER-CARFAGNI	Università degli studi di Parma, Italy
DAVID STEIGMANN	University of California at Berkeley, USA
PAUL STEINMANN	Friedrich-Alexander-Universität Erlangen-Nürnberg, Germany

ADVISORY BOARD

J. P. CARTER	University of Sydney, Australia
D. H. HODGES	Georgia Institute of Technology, USA
J. HUTCHINSON	Harvard University, USA
D. PAMPLONA	Universidade Católica do Rio de Janeiro, Brazil
M. B. RUBIN	Technion, Haifa, Israel

PRODUCTION production@msp.org

SILVIO LEVY Scientific Editor


Cover photo: Ev Shafir

See msp.org/jomms for submission guidelines.

JoMMS (ISSN 1559-3959) at Mathematical Sciences Publishers, 798 Evans Hall #6840, c/o University of California, Berkeley, CA 94720-3840, is published in 10 issues a year. The subscription price for 2017 is US \$615/year for the electronic version, and \$775/year (+\$60, if shipping outside the US) for print and electronic. Subscriptions, requests for back issues, and changes of address should be sent to MSP.

JoMMS peer-review and production is managed by EditFlow® from Mathematical Sciences Publishers.

PUBLISHED BY

 **mathematical sciences publishers**
nonprofit scientific publishing

<http://msp.org/>

© 2017 Mathematical Sciences Publishers

Special issue on Coupled Field Problems and Multiphase Materials

Preface	CORINA S. DRAPACA, STEFAN HARTMANN, JACEK LESZCZYŃSKI, SIVABAL SIVALOGANATHAN and WOJCIECH SUMELKA	1
Variational methods for the solution of fractional discrete/continuous Sturm–Liouville problems	RICARDO ALMEIDA, AGNIESZKA B. MALINOWSKA, M. LUÍSA MORGADO and TATIANA ODZIJEWICZ	3
Analytical and numerical solution of the fractional Euler–Bernoulli beam equation	TOMASZ BLASZCZYK	23
Fractional calculus in neuronal electromechanics	CORINA S. DRAPACA	35
Time-adaptive finite element simulations of dynamical problems for temperature-dependent materials	MATTHIAS GRAFENHORST, JOACHIM RANG and STEFAN HARTMANN	57
Computer simulation of the effective viscosity in Brinkman filtration equation using the Trefftz method	JAN ADAM KOŁODZIEJ, MAGDALENA MIERZWICZAK and JAKUB KRZYSZTOF GRABSKI	93
Numerical simulations of mechanical properties of alumina foams based on computed tomography	ZDZISŁAW NOWAK, MARCIN NOWAK, RYSZARD PEŁCHERSKI, MAREK POTOCZEK and ROMANA ŚLIWA	107
Gradient-enhanced large strain thermoplasticity with automatic linearization and localization simulations	JERZY PAMIN, BALBINA WCISŁO and KATARZYNA KOWALCZYK-GAJEWSKA	123

